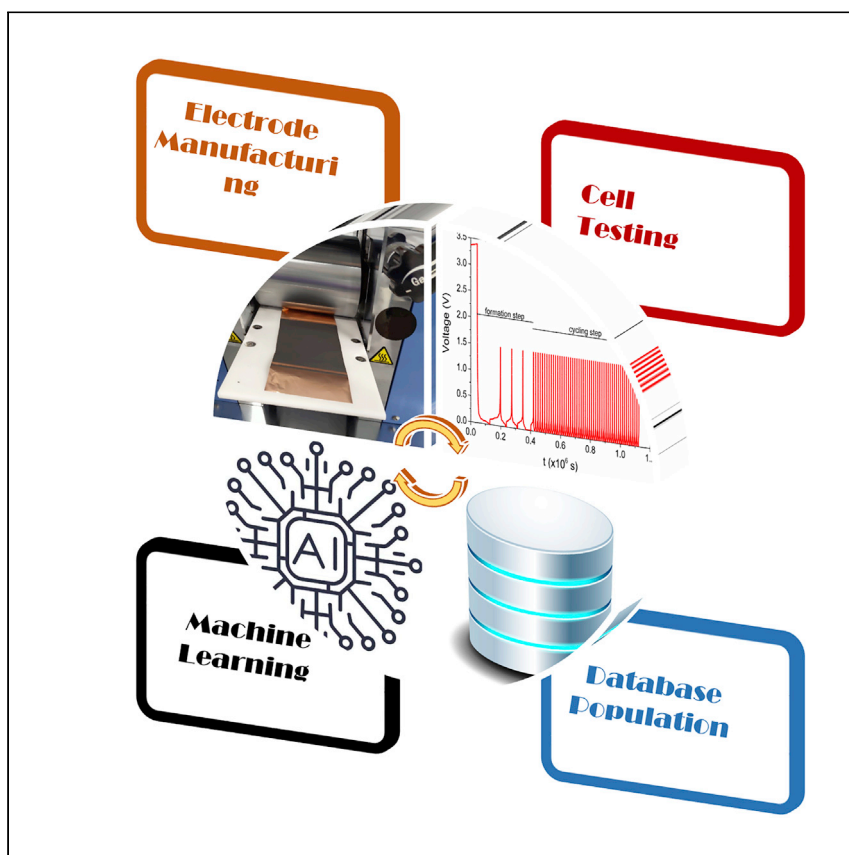


Article

Formulation and manufacturing optimization of lithium-ion graphite-based electrodes via machine learning



Optimization of the manufacturing procedure for Li-ion batteries is a major issue in the scientific and commercial battery world. Drakopoulos et al. develop graphite-based anode electrodes and employ artificial intelligence (AI) to link the manufacturing protocols to the final electrochemical and cycle life performance parameters.

Stavros X. Drakopoulos,
Azarmidokht
Gholamipour-Shirazi, Paul
MacDonald, ..., Gareth J.
Conduit, Alexandru Cazacu,
Emma Kendrick

e.kendrick@bham.ac.uk

Highlights

High-coat-weight, graphite-based electrodes developed for high-energy applications

Physical and cell performance property relationships used for optimization

A database is designed for extraction and analysis of data

Data model is trained and employed as a predictive tool for cell optimization

Article

Formulation and manufacturing optimization of lithium-ion graphite-based electrodes via machine learning

Stavros X. Drakopoulos,¹ Azarmidokht Gholamipour-Shirazi,¹ Paul MacDonald,² Robert C. Parini,³ Carl D. Reynolds,¹ David L. Burnett,^{1,4} Ben Pye,¹ Kieran B. O'Regan,^{1,4} Guanmei Wang,² Thomas M. Whitehead,³ Gareth J. Conduit,^{3,5} Alexandru Cazacu,² and Emma Kendrick^{1,6,*}

SUMMARY

Understanding the formulation and manufacturing parameters that lead to higher energy density and longevity is critical to designing energy-dense graphite electrodes for battery applications. A limited dataset that includes 27 different formulation, manufacturing protocols, and performance properties is reported. Input parameters from formulation and manufacturing are varied: slurry composition, mixing protocol, electrode coating gap size, drying temperature, coating speed, and calendaring. Measurable outputs from the rheological characteristics, adhesion, and electrochemical testing are recorded. A database with the inputs and output parameters is populated and used to train an artificial intelligence model. Validation of the model is performed upon test data and an optimized electrode formulation and manufacturing process predicted. The electrode manufactured using the model process shows excellent cycle life and capacity agreement to prediction. The data model can be used to predict and design the formulation and manufacturing process to produce thick, high-coat-weight, graphite-based electrodes.

INTRODUCTION

The Li-ion battery (LIB) has initiated a revolution in power electronics, and there has been an exponential increase in demand,¹ in part due to the new market in electric vehicles.^{2,3} High-throughput methods are under development to accelerate the optimization process of battery materials in terms of synthesis, manufacturing, and electrochemical performance.^{4–7} Manufacturing governs battery properties, including energy density, cycle life, and cost. The fabrication of Li-ion batteries is divided into three basic categories: (1) ink preparation (slurry-based composite that contains the active material, solvent, binder, conductive additive, and dispersant); (2) manufacturing (mixing, coating, drying, and mechanical compression-like calendaring); and (3) cell assembly.⁸

Graphite is widely used in Li-ion batteries due to its stability and long-cycle life.⁹ Various efforts have investigated adding additives to electrodes in order to increase mechanical durability, adhesion properties with the current collector, electrical conductivity, and longevity.^{10,11}

The high electronic conductivity of graphite results in low impedance and electrode polarization when dispersed within a 3D conductive network.^{12,13} Carbon black is

¹The Energy Materials Group, School of Metallurgy and Materials, University of Birmingham, Birmingham B15 2TT, UK

²Ansys UK Limited, 300 Rustat House, 62 Clifton Road, Cambridge CB1 7EG, UK

³Intellegens Limited, Eagle Labs, 28 Chesterton Road, Cambridge CB4 3AZ, UK

⁴The Faraday Institution, Harwell Campus, Didcot OX11 0RA, UK

⁵Theory of Condensed Matter Group, Department of Physics, University of Cambridge, Cambridge CB2 1TN, UK

⁶Lead contact

*Correspondence: e.kendrick@bham.ac.uk
<https://doi.org/10.1016/j.xcrp.2021.100683>



often used; when processed correctly, it forms chains of conductive beads that form electronic wires between graphite particles, enabling fast electron transfer through the electrode.¹⁴ Other carbons, such as carbon nanotubes (CNTs),^{15,16} graphene, and carbon fibers,¹⁷ can also improve electrical and thermal conductivities.^{9,11,17,18}

To optimize electrode performance, formulation, active: binder: conductive carbon: solvent ratio, is important.¹⁹ Polyvinylidene fluoride in N-methyl-2-pyrrolidone (PVDF-NMP) binder-solvent combinations give high mechanical and electrochemical stabilities; however, due to the toxicity of NMP and the difficulty in PVDF removal at end of life, other binder systems, such as carboxy methyl cellulose and styrene butadiene rubber (CMC-SBR) in water, are being investigated.^{20–23} To maximize energy density, minimum quantities of binders and conductive additives are used while maintaining good electrical and mechanical properties.²⁴

The manufacturing process includes four basic steps, mixing, coating, drying, and calendaring. The mixing parameters, including the composition, rotation speed, mixing time, and temperature, directly affect the mixing shear rate and the resultant slurry viscosity and thus the dispersion of each component.^{8,25} Electrode coating is dependent upon gap size and coating speed, which also affects the porosity and coat weight of the electrode coating.²⁶ An optimum porosity is required such that ions can be transported through the electrolyte in the electrode pores and electrons can be transported from the site of electrochemical reaction to the current collector. Previous work indicates the optimum porosity for graphite is 35% for high-energy applications.²⁷ Low porosities improve electronic conductivity but block the Li-ion diffusion.^{28,29} Optimized drying of the electrode results in strong adhesive and cohesive bonding, controlled via temperature and time.^{30–32} Finally, calendaring is performed to optimize porosity level and improve the electronic wiring of the particles to the current collector.^{29,33}

Often design of experiments (DOE) is used in industry to optimize the manufacturing process. If a full factorial approach was used, a DOE containing 4 replicates of 5 factors (formulation, coating gap size, coating speed, drying temperature, and calendaring) with 3 levels each apart from calendaring that has 2 levels would result into $4 \times 3^4 \times 2^1 = 648$ cells; this number can be reduced with different experimental designs.³⁴ However, factors outside of the experimental control matrix can occasionally affect the electrode outputs, i.e., humidity and temperature. More recently, machine learning or artificial intelligence (AI) methods have been used;^{35–40} examples include the optimization of a lithium nickel manganese cobalt oxide (NMC) electrode,⁴¹ the utilization of more in-depth electrochemical diagnostic methods,⁴² and the modeling of battery safety risks.⁴³ In research, the electrode development process is more intuitive, as electrochemical testing takes a very long time to complete (several weeks or months), and often, the number of available test channels is the biggest limitation. An approach to learn more from these smaller datasets, and to fill in potential gaps in the data, is to use machine learning and data-driven modeling methods. Alchemite is a self-consistent, iterative machine-learning algorithm that has been applied to a wide range of domains, including battery state prediction,⁴⁴ superalloy design,⁴⁵ and pharmaceuticals.⁴⁶ Alchemite is an adaptation of a neural network but with all inputs also being predicted so is surrounded by an iterative imputation cycle to handle missing data. The architecture of the Alchemite algorithm is shown in [Figure S5](#) and described elsewhere.^{46–48}

In this work, we demonstrate the effectiveness of a data-driven model on a small research dataset with an aim to obtain high-energy-density graphite electrodes. A

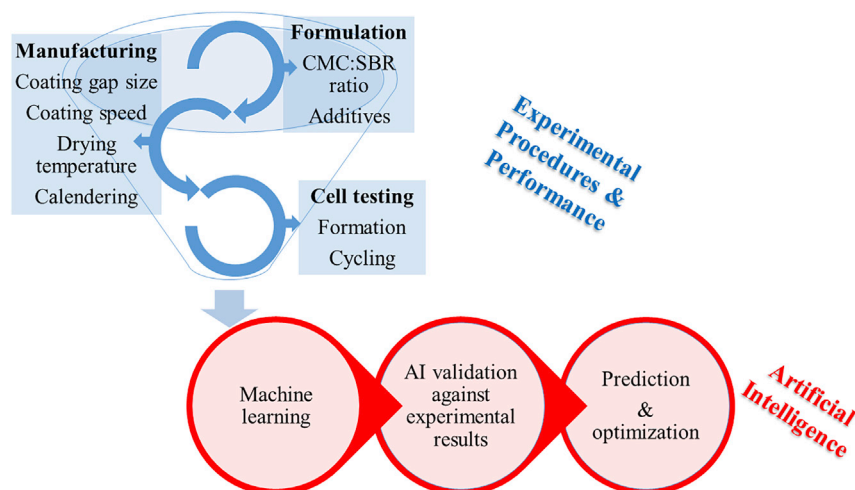


Figure 1. Schematic overview

A schematic overview of the present study for graphite electrode formulation and manufacturing, with the investigated parameters

series of experiments, with a focus on low-cost and low-environmental-impact manufacturing processes, were performed to maximize coulombic efficiency, capacity, and cycle life. A full DOE was not performed; instead, a small research dataset was produced from a series of different formulations and manufacturing optimizations. The data are further processed via a data-driven model (Alchemite) in order to provide additional insight, and an optimized electrode was designed using a Bayesian optimization process. 27 different graphite electrode formulation and manufacturing protocols (cases) were developed to optimize the cycle life performance of anode electrodes for high-energy applications. The effect of CMC:SBR ratios and additives upon discharge capacity and cycle life was investigated. Subsequently, the effect of the manufacturing steps (coating blade gap size, coating speed, drying temperature, and calendering) upon the electrode properties (porosity and adhesion normal force) was investigated. A schematic overview of this analysis is provided below in [Figure 1](#).

A further aim is to establish relationships between manufacturing and cell performance. Currently, empirical design of experiments concludes with the electrochemical performance of a cell. Physical property – performance relationships will help to accelerate this electrode optimization process.

In this work, graphite (BTR) and carbon black (C45) electrodes were developed as a test case. Binding materials carboxymethyl cellulose (CMC) and styrene-butadiene rubber (SBR) were mixed at various ratios (2:1, 1:3, and 2:3) at 3.00% by electrode mass. Additives (0.5% w/w) to improve conductivity were investigated: long and short CNTs; carbon fibers; and DSA (hydrophobic dispersant). After the slurry formulations (55% w/w solid) were mixed, the rheological properties were recorded. The inks were coated onto a copper current collector, at coating gap size (70–300 μm), coating speeds (0.1–0.5 m/min), and drying temperature (60°C–120°C), before calendering or not. Adhesion was measured using a 180-degree peel off test. Cell testing was performed against Li metal in a coin cell configuration and formation (one C/20 discharge-charge cycle and three C/10 cycles) and fast cycling (50 cycles discharged at C/2 and charged at C rates) performed. C rate is 350 mAhg^{-1} at 0.1C. In total, 256 cells were made and the outliers were discarded. Outliers were determined as cells that did not complete

Table 1. Graphite electrode characteristics. Graphite electrode manufacturing details electrode and cell characteristics, with corresponding predicted and actual specific capacity after 30 cycles.

Case no.	Formulation no. (Table S1)	Drying temperature (°C)	Coating speed (m/min)	Coating gap size (μm)	Calendering	Porosity (%)	D30 experimental (mA.h/g)	D30 predicted (mA.h/g)	RMSE (mA.h/g)
40	6	60	0.2	150	NO	52.3	197.3	277.8 ± 34	42.5
41		60/80				54.3	205.1	255.5 ± 37	29.7
47		80/100	0.4			53.7	241.1	268.7 ± 45	46.1
48					YES	32.0	321.9	285.5 ± 34	43.6
60		60	0.2	200		28.5	109.5	148.6 ± 52	32.6
16	3	80	0.1	140		22.4	310.2	319.2 ± 17	12.8

The root mean-squared error (RMSE) values are averages over the cycle life between the experimental and the predicted specific capacity values. All the cells presented are characterized by a CMC/SBR ratio of 2:3.

formation or the 50 cycles. The Ansys Granta MI software has been used to collect materials, cell manufacturing processes, and test data by means of a set of customized data importers. A data model was trained on the data from 85 cells, a further 6 cells from different manufacturing conditions to the training data (Table 1) provided a dataset that the model was tested against. The 85 cells used for the training were chosen because they completed the cycle life test. The 6 test cells were selected because they had been produced and tested after the original 85 cells in similar but different manufacturing conditions (Table 1). 3 cells were made based on the AI-designed electrode process and formulation.

Standard operating procedures for all the manufacturing and testing processes have been established, including storage.⁴⁹ With small-batch processing of inks and draw-down coatings, a slight variability in coat weight is observed as the weight of the ink decreases as it is pulled down the coating. This variation affects the calendering pressure across the electrode and hence the porosities. However, to limit variation, only electrodes with similar coat weights, thicknesses, and porosities are tested (maximum 10% difference). Three to five cells are tested from every manufacturing case, and any outliers are removed. A summary of the physical and electrochemical properties of electrodes in each cell is available (Mendeley dataset: <https://data.mendeley.com/datasets/4dh2h3tsf4/draft?a=301e2177-92bf-4929-899f-ef53d9ae956f>). More information about the formulation, manufacturing steps, testing methods, and coin cell assembly can be found in the [supplemental experimental procedures](#) and [Tables S1](#) and [S2](#).

RESULTS

Formulation variations

To weigh the importance of the various constituents present in a graphite-based anode coating toward higher discharge capacities and longer cycle lives, different CMC:SBR formulation (open symbols) and additive (closed symbols) variations were examined, as presented in [Figure 2](#). A Gaussian process regression (GPR) was applied to all the data using an RBF kernel with length scale set to the standard deviation of the independent variable for each plot. In [Figure 2A](#), the discharge-specific capacity at the 5th cycle is plotted against the 30th cycle (D5 versus D30) to show both the cell performance and the cycle life of the cells, which have been manufactured at the same conditions (coating speed, temperature, and gap size). During the cycling step, the cells were discharged at C/2 and charged at C. In this case, none of the electrodes were calendered; therefore, the corresponding porosity values all lie in the range of 50%. According to [Table S1](#) presented in [supplemental information](#), the three compared ratios have graphite (BTR) and carbon black (C45) concentrations at 94.5% w/w and 2.5% w/w, respectively, and also constant binding agents'

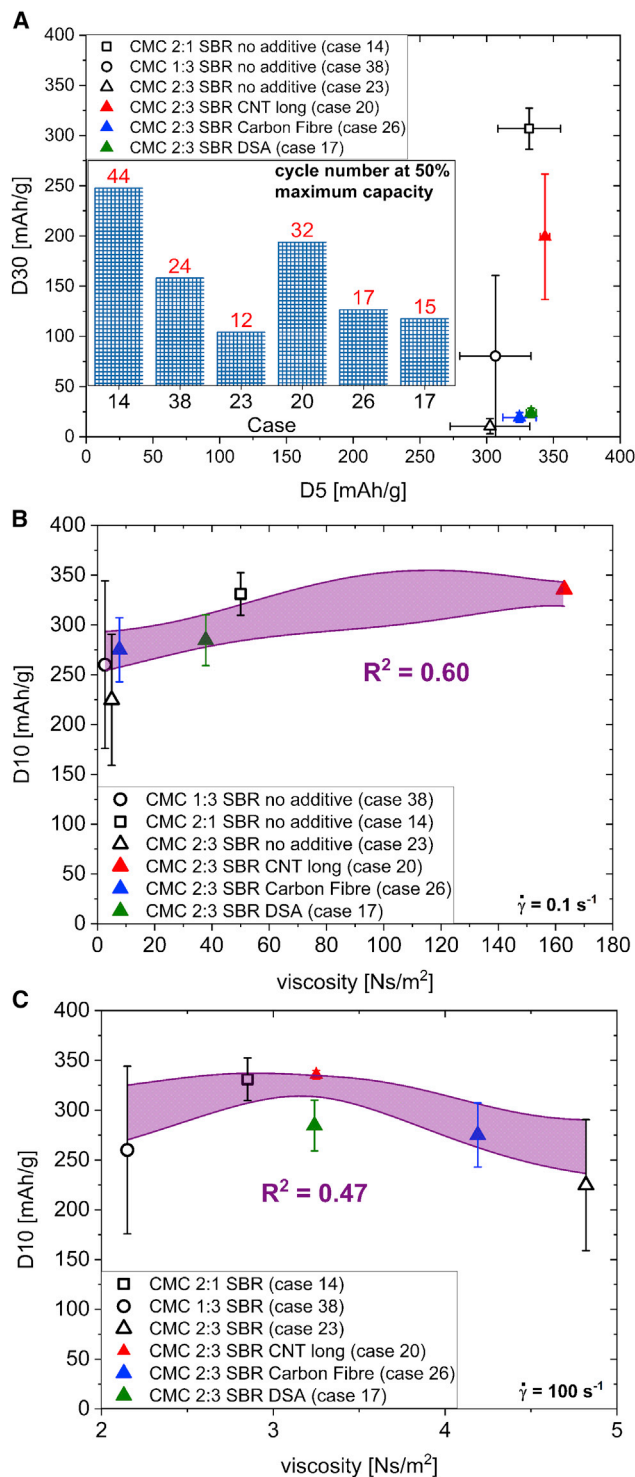


Figure 2. Discharge-specific capacity performance of the formulations under study at the same manufacturing conditions

(A) Discharge-specific capacity at cycle number 30 against cycle number 5 examining the different CMC:SBR ratios and various additives, with an inset for the cycle number at 50% maximum capacity.

sum at 3.0% w/w. Given that the polymeric binders are resistive materials, at higher mass fractions, their presence increases the internal resistance of the cell, hindering thus the Li-ion diffusion, resulting in shorter cycle life.⁵⁰ Therefore, it is crucial to include as little binder as possible, without compromising the mechanical stability of the electrode.⁵¹ Within the same graph, a comparison of different materials as additives with a CMC 2:3 SBR ratio and a total conductive additive of 2.5% w/w is also given (DSA is a non-conductive dispersant for hydrophobic materials, used here to limit the aggregation of carbon black particles).

At first, the various CMC:SBR ratios (Ashland and Zeon) cells are presented with open symbols, with the best performing sample (CMC 2:1 SBR) to contain the highest weight percentage of CMC (2% w/w), which, according to the literature, is the critical low concentration for CMC to form a network to support the stability of the anode.⁵² The specific capacity of the electrode containing the 2CMC:1SBR ratio reached on average 320 mA.h/g right (D5) and achieved 50% of the initial capacity at 44 cycles, according to Figure 2A. The 1CMC:3SBR ratio exhibited a lower D5 discharge capacity, at approximately 310 mA.h/g, and a faster decline over cycle number, 50% of capacity lost at 24 cycles. The shortest cycle life was observed for the 2:3 ratio, which exhibited a 50% drop after 12 cycles and a 90% drop from the maximum capacity at 25 cycles. Moving forward to the effect of additives (closed symbols) on the worst performing 2CMC:3SBR ratio, it is evident that all have a beneficial effect in both D5 and D30 values. At first, it is visible that the DSA dispersant has a beneficial effect in cycle life when comparing it with the no additive sample (both contain approximately 2.5% w/w C45 conductive additive), leading to twice the D30 values than that of the no additive formulation, indicating more effective dispersion of C45 in the slurry. Considering the performance of electrodes containing additional conductive additives, the formulation with the highest cycle life retention is the 0.5% w/w long CNTs electrode, which achieves half its initial capacity at the 32nd cycle. In addition, at its 5th cycle, it reaches a discharge-specific capacity of almost 350 mA.h/g against 300 mA.h/g of the electrode without the CNTs. CNTs and carbon fibers have a high tensile strength and high aspect ratio for electronic conductivity, which facilitates the electron transport.⁵³ The addition of carbon fiber to the formulation improves the capacity retention with respect to the 2:3 CMC:SBR no additive electrode but to a lesser degree than those produced containing CNTs.

Having discussed the cycling performance of the various CMC:SBR ratios and different additive containing cells in Figure 2A, the 10th discharge capacity after formation (D10) as a function of the slurry's viscosity is presented at Figure 2B in order to determine the relationship between the cycle life and the slurry properties (prior to electrode coating and cell preparation). The rheological experiments were conducted at room temperature and at a shear rate of $\dot{\gamma} = 0.1 \text{ s}^{-1}$. For this analysis, different formulations were investigated, no calendaring was applied to the coated anodes, and the manufacturing conditions were identical (gap size, coating speed, and coating temperature). The highest D10 values are observed in the presence of CNTs, which are expected to facilitate charge transport by inducing a conductive network and increase the slurry viscosity due to their mechanical durability. Ink viscosity could be an important early indicator for electrode mechanical stability and ultimate cell life. Figure 2B illustrates a correlation between high viscosity at low

(B and C) The discharge-specific capacity at cycle number 10 (D10) is presented as a function of anode slurry viscosity as obtained by shear rate rheology experiments at shear rates of (B) 0.1 s^{-1} and (C) 100 s^{-1} . The R^2 values of the GPR fittings are included in (B) and (C). The error bars are calculated based on the standard deviation.

shear (0.1 s^{-1}) and higher capacity and longer cycle life. The 0.1 s^{-1} shear rate is representative of the zero-shear viscosity of the slurries and thus indicates how the ink structure behaves prior and after coating. The higher viscosities, at this particular solid content, could indicate the optimum carbon black dispersion. If over-dispersed, the carbon doesn't provide the 3D internal network and the inks are often less viscous, whereas under-dispersed, the carbon black is aggregated. Better dispersion within the slurry during mixing leads to enhanced stability of the particle suspension and improved slurry quality. When comparing the cell performance in the presence of dispersive and conductive additives for the CMC 2:3 SBR formulations (open and closed triangles), it is clear that these additives increase the viscosity of the slurry and indicate good dispersion. As expected, with increasing CMC content, the viscosity of the slurry increases, which is in agreement with a similar trend observed at 1 s^{-1} shear rate (Figure S4A). The viscosity values of the slurries, as obtained from the rheological measurements, decrease with increasing shear rates. At 10 s^{-1} (Figure S4B), the viscosities showed no trend with capacity, but at 100 s^{-1} , presented in Figure 2C, it appears that capacity is decreasing at higher viscosities, indicating that, at coating shear rates, lower viscosities are preferable as the slurries are more easily coated. In addition to the viscosity increase, the electrodes produced from the CNT and carbon fiber additives show higher capacities with the CNTs containing cell exhibiting a reduced resistance according to Table S2.

Manufacturing conditions

In this section of the paper, the electrode-preparation steps, namely coating, drying, and calendaring, were examined to determine the optimal manufacturing conditions that will result into the highest capacity retention. At first, the physical properties of the examined electrodes as a function of coating gap size and drying temperature are presented (Figures 3A–3C), with the electrochemical cell performance following (Figure 3D). A relationship between the manufacturing inputs, physical properties, and the cell performance is elucidated. Finally, the effect of calendaring is examined (Figure 4) upon the cycle life performance varying the CMC:SBR ratios (1:3, 2:1, and 2:3).

In Figure 3, the effect of the coating (doctor blade) gap size and drying temperature manufacturing conditions during the electrode-coating process were examined, and the relationship of these variables in process related to changes in the physical (electrode thickness, porosity, and adhesion) and electrochemical characteristics (cycle life and resistance) of the electrodes. The formulation of the cells examined in this section was kept constant at a CMC:SBR ratio at 2:3 with only C45 conductive additive at 2.5% w/w, and none of the anode electrodes underwent any calendaring in order to isolate the contribution of the coatweight and drying temperature on the cell performance.

As is expected, as the blade gap increases, the thickness and coat weight of the coating also increases, as more slurry is deposited onto the current collector (Figure 3A). Drying temperature, however, also affects the thickness of the electrode, and by the drying temperatures to 120°C , the porosity (and thickness) decreases (Figure 3B). This increase in electrode density results in improved electrochemical properties, with greater capacities at D30 being observed (Figure 3D). Interestingly, even without calendaring, porosity values as low as 25% can be achieved, although this effect is limited with higher coatweights, and for gap sizes over $200 \mu\text{m}$, the porosity values are almost independent of temperature and exceed 50%. The 35% porosity aim²⁷ was observed in the gap size range of around $100 \mu\text{m}$. Figure 3C shows the dependence of drying temperature and coating gap size upon the adhesion normal force as defined by the delamination force between the coated anode and the copper current collector. For gap sizes above $200 \mu\text{m}$, the adhesion normal

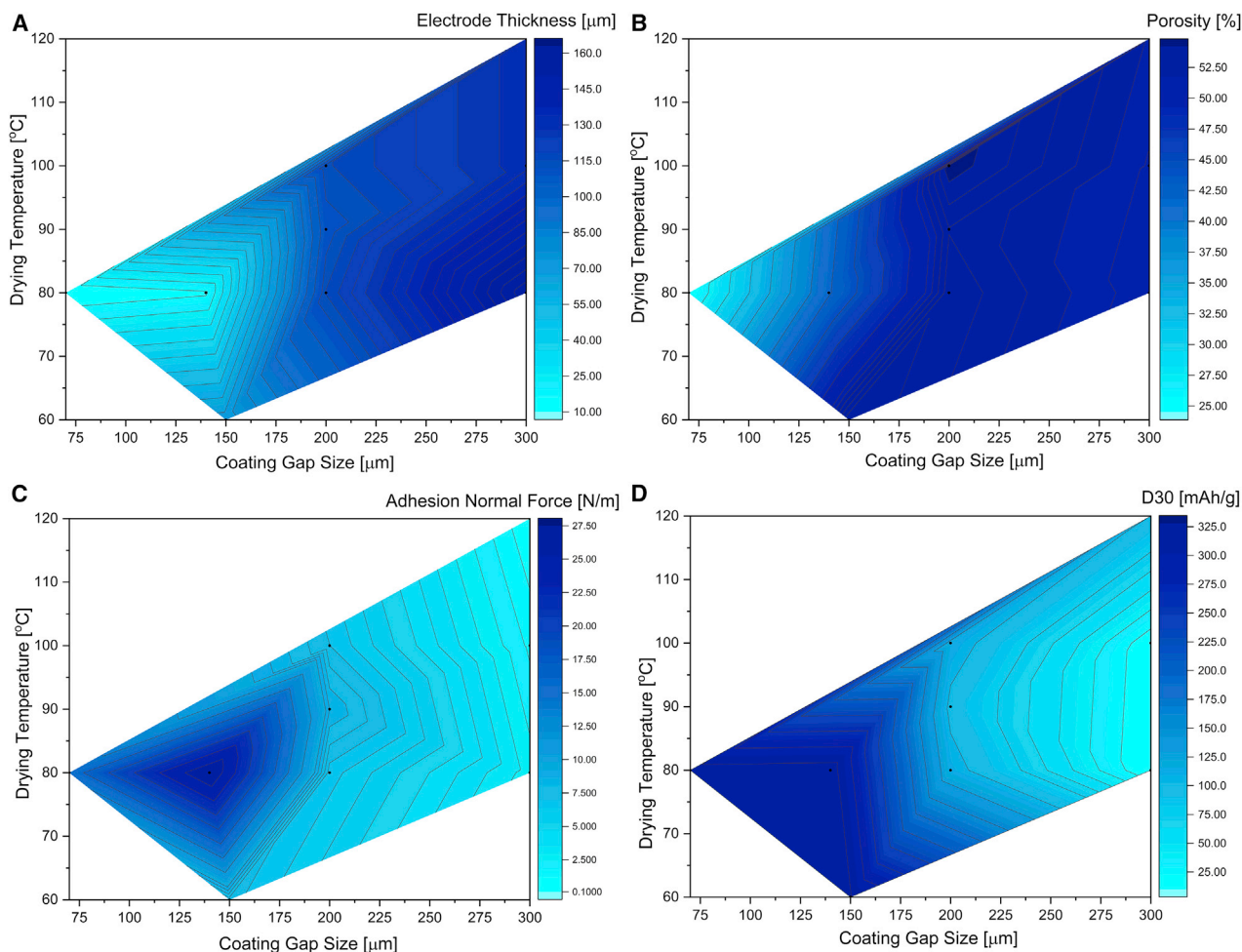


Figure 3. Electrode manufacturing conditions as opposed to physical and electrochemical properties

Contour plots for uncalendared electrodes evaluating the changes in drying temperature and coating gap size with the physical and electrochemical properties (A) electrode thickness, (B) porosity, (C) adhesion normal force, and (D) discharge-specific capacity at the 30th cycle (D30).

force values are low (below 10 N/m), indicating poor physical connection between the graphite particles and the current collector. The low adhesion normal forces are directly related to high porosity values, indicating that this is due to the smaller contact area between the graphite particles and copper.³⁰ This observation also suggests that the adhesion can be directly related to the contact resistance of the coating and hence polarization of the electrodes relating to the ohmic resistance (IR drop), which will be discussed later (Figure 8F). Below 200 μm , the highest adhesion normal forces were observed at 80°C and 140 μm , for which the highest cycle life was also observed, constituting the optimum manufacturing conditions.

In Figure 3D, a contour plot that combines the drying temperature and coating gap size with the discharge specific capacity at the 30th cycle (D30) is presented. It is notable to mention that the D30 values range from 15 up to 340 mA.h/g, and thus, manufacturing plays a vital role on the resulting performance. The most important factor, similar to what was discussed previously, is the coating gap size, which above 200 μm gives D30 values below 100 mA.h/g. Below 150 μm , high D30 values were achieved that mostly exceeded 300 mA.h/g and are jointly attributed to the low porosity and high adhesion normal forces discussed in Figures 3B and 3C,

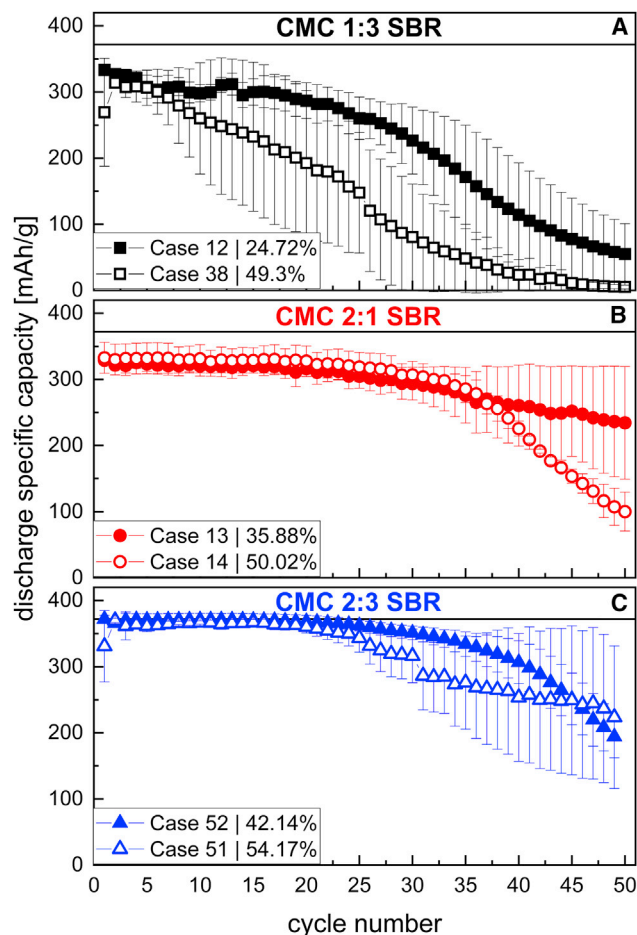


Figure 4. The effect of calendaring

Cycle life of (A) CMC 1:3 SBR, (B) CMC 2:1 SBR, and (C) CMC 2:3 SBR, exploring the effect of calendaring (solid symbols and open symbols correspond to calendared and non-calendared anode electrodes, respectively). The average porosity values are included within the legends for all the samples under study. A solid line at 372 mA.h/g is given within each graph to highlight the theoretical specific capacity value for graphite. The error bars are calculated from standard deviation.

respectively. Additionally, the vastly different performances observed by varying the gap size are also due to the very fast lithiation and delithiation cycles (C and C/2, respectively) that are not ideal for the thicker samples, because Li ions need to cover greater distances during lithiation and delithiation due to diffusion limitations that affect the electrochemical reaction within the cell.^{26,54,55} The same charge and discharge protocol was employed in all cases, so the data-driven model has less variables to work with. Also, cells with higher thicknesses have a higher internal resistance that decreases the power output and increases polarization, resulting in ohmic losses (heat) that can contribute to deterioration in the observed capacity over time.²⁶ Although drying temperature does not appear to contribute much in the battery performance at lower gap sizes, at high thicknesses, it is observable that the D30 values are 4 times higher at 120°C than at 80°C, which is attributed to more efficient solvent evaporation at higher temperatures.

Three CMC:SBR ratio variants were chosen to examine the effect of calendaring, and the comparison with the non-calendared sample is presented in Figure 4. It is

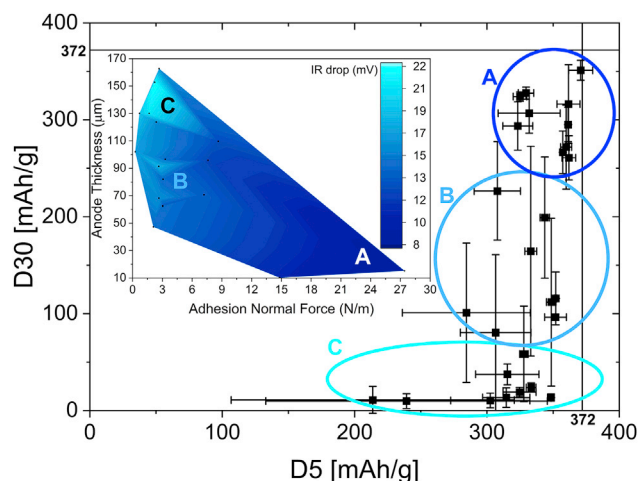


Figure 5. The cycle life performance of all the cells under study and its relation to electrode manufacturing, adhesion properties, and internal resistance

Discharge-specific capacity at cycle number 30 against cycle number 5 plotting all examined cases. As an inset, a contour plot is presented, combining information for the anode thickness, the adhesion normal force, and the IR drop. The circles' colors correspond to the heatmap of the contour plot (also noted as areas A, B, and C, corresponding to increasing values of IR drop, respectively). The error bars are calculated based on the standard deviation.

evident from all the samples that calendaring decreases significantly the porosity values and increases the cycle life of the cells, attributed to the changes in the porous structure that diminishes the ohmic contact resistance of the coating.²⁸ Figures 4A and 4B show that calendaring significantly affects the cycle life of the cells to the point that, at the 50th cycle, over double values of discharge-specific capacity are observed. Interestingly, the porosity values after calendaring vary a lot (from 25% to 42%), affecting thus in a different way the calendared cells, with the more effective calendaring (greater porosity drop) to increase the capacity retention of the cells. The variation in the porosities is a result of different degrees of calendaring in order to provide a greater range of values during the data-driven modeling analysis.

A summary of all 27 cases investigated in this paper is presented in Figure 5 in a D30 versus D5 representation of the data. It is clearly visible that, although most cells exhibit values of $D5 \geq 300$ mA.h/g, there is a great variation in D30 values that range from 350 down to 10 mA.h/g and strongly depend on the formulation and manufacturing characteristics and conditions as discussed in the previous sections of the paper. The data were grouped into three categories (A, B, and C) based on their D30 values: $D30_A > 250$ mA.h/g; 100 mA.h/g $< D30_B < 250$ mA.h/g; and $D30_C < 100$ mA.h/g, respectively. As an inset to Figure 5, there is a contour plot that summarizes information gathered from three different aspects of cell performance: the electrode thickness; the adhesion normal force; and the IR drop (the IR drop being indicative of the series resistance of the cell). The electrode thickness is a property that can be controlled in the initial stages of coating through the gap size, and the adhesion normal force can be tested right after drying. Evidently, these two easily controlled and measured parameters have an important effect on the IR drop and the internal resistance of the cell and immensely affect the resulting battery performance and the cycle life, as the colored circles indicate, chosen to match the heatmap for the IR drop variation in the contour plot. Therefore, an optimization process can be achieved faster by controlling the aforementioned properties, without having to invest a lot of resource into the process.

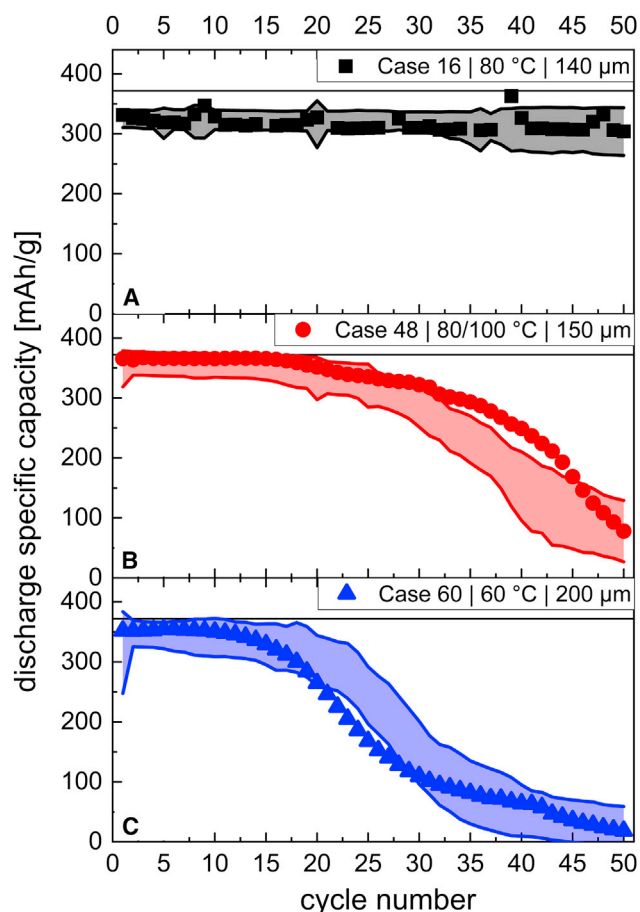


Figure 6. Testing the Alchemite model predictions against experimental data

Examples of the cycle life of the experimental (symbols) against the predicted values, including the uncertainties (colored areas). All the test cells had a CMC:SBR ratio of 2:3. The coating gap size and the drying temperature for each are given within each graph. A solid line at 372 mA.h/g is given within each graph to indicate the theoretical specific capacity of graphite. In addition to the presented 3 validation cells, another 3 are given in [Table 1](#).

Data-driven model development

The data from 85 cells (27 cases), with 15 experimental variables (listed in [Table 1](#)), were used to train a single Alchemite machine-learning model. The model was tested against the outputs from 6 cells generated after the training data, providing a test of the realistic, prospective application of the machine-learning model, independent of the training data.

The effectiveness of the model is shown in [Figure 6](#), where the predicted discharge-specific capacities are compared to the experimental for 3 cases, although the remaining cases are given in the [supplemental information in Table 1](#), including summary statistics on the predictive accuracy. In [Figure 6](#), the shaded areas represent the standard deviation prediction intervals and the experimental results are shown as colored points. The chosen cells as depicted in [Figure 6](#) had a CMC 2:3 SBR ratio and underwent calendaring although they were characterized by different coating gap sizes, coating speeds, and drying temperatures. The full formulation and manufacturing characteristics of the 6 test cells are provided in [Tables S1](#) and [S3](#). In all cases, high agreement between the predicted and experimentally observed

discharge curves is obtained. In particular, the first test cell, case 16 (140 μm blade gap size; 80°C drying temperature) shown in [Figure 6A](#) is exhibiting discharge-specific capacity values in the range of 300 and 350 mA.h/g, where no signs of significant capacity deterioration are visible at the observable cycle life window. The Alchemite model was able to re-create successfully the experimental behavior as with the other two test cells, case 48 (150 μm blade gap size; two-step 80/100°C drying temperature) and case 60 (200 μm blade gap size; 60°C drying temperature) presented in [Figures 6B](#) and [6C](#), respectively. In those cases, the early falloff in capacity is correctly identified by the Alchemite model, and the high-cycle-number behavior is also accurately predicted. Comparisons with standard machine-learning approaches (lasso and random forests) are provided in [Figure S6](#) and [Table S4](#).

As well as the expected value of the predictions from the machine-learning approach, it is important that the uncertainty in the predictions is well understood. This uncertainty can come both from variability in the experimental measurement procedures used to generate the model training data as well as extrapolation in the formulation space when making predictions. To analyze the uncertainties in the predictions, in [Figure 7](#), we plot histograms of the distribution of predictions from Alchemite for the specific capacity after 30 cycles of the three test cells also examined in [Figure 6](#). We observe a tightly peaked distribution for case 16, where the specific capacity is not varying rapidly as a function of cycle number and the machine learning is confident of its prediction. In contrast, for case 60, the distribution has wide-ranging tails that indicate disagreement among the different neural networks that form the Alchemite architecture and hence reduced confidence in the predictions. The distribution for case 60 also has positive skew (third standardized moment 1.08), providing more detail about the model's understanding of the dataset (for instance, that it expects the lower limit on capacity at this number of cycles for this cell to be harder than the upper limit, as some constituent neural networks can model quite high capacity for this cell). The standard deviation across these distributions of predictions generates the prediction intervals shown in [Figure 6](#).

Physical properties and Alchemite as predictive tools

The fundamental scope of the present paper is to establish tools to predict the cycle life performance after changes in the manufacturing procedures avoiding the time-consuming and costly full electrochemical characterization. The effort showed here is to relate non-electrochemical testing (slurry rheology and adhesion experiments) to the cell performance and how this in-depth understanding of the manufacturing-performance relationship can develop data-driven modeling using the Alchemite software. From the accumulated data for the high-coat-weight graphite electrodes manufacturing, the aim was to provide evidence relating measured properties and outputs to the electrochemical performance. If the performance can be predicted from the input data, i.e., specific measured attributes during the manufacturing processes, the time for any new electrode and cell development would be reduced, and the lengthy electrochemical cycling tests are not required. The trained data model above shows that, with a limited dataset, this is indeed possible, and accurate predictions of cycle life can be achieved. To understand the effect of the formulation and process upon the final cell performance, the chemical and physical relationships of the changes in the manufacturing processes need to be understood. Here, the relationship of the physical changes that are observed in the inks and electrodes, through metrology measurements, are linked with the final performance properties, capacity, cycle life, and resistance. [Figure 8](#) shows that the empirical analysis can elucidate relationships between the physical and electrochemical properties. Having built confidence in the predictive

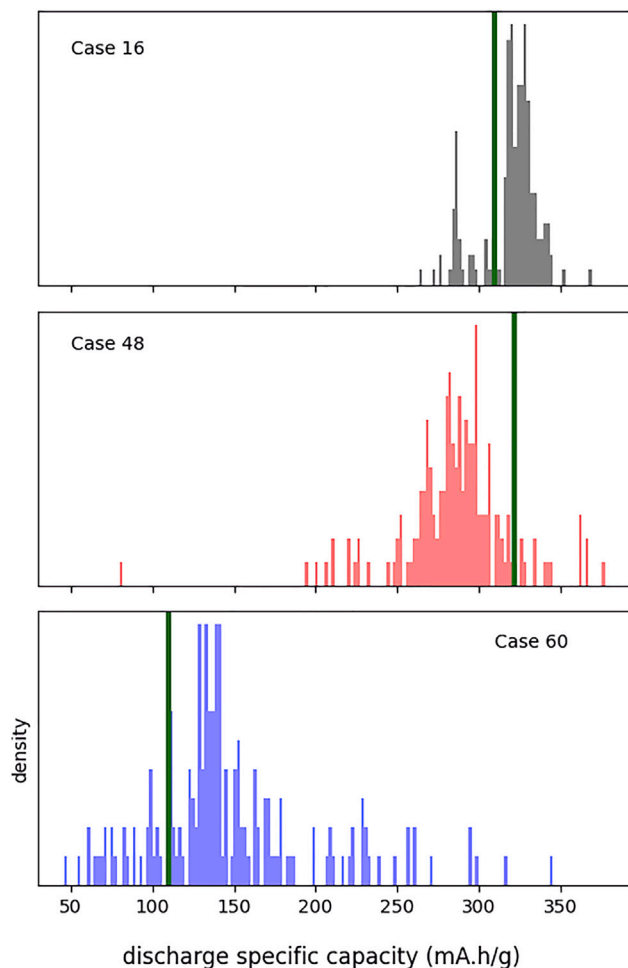


Figure 7. Uncertainties in the predictions

Examples of the uncertainty in the predictions of the discharge-specific capacity after 30 cycles (D30) showing histograms of the distribution of model predictions and, as dark green vertical lines, the measured experimental values

performance of Alchemite, a graphite electrode formulation and manufacturing process that achieves a high specific capacity after 30 cycles (D30) of over 150 mA.h/g using an active mass of greater than 25 mg was designed by the machine-learning model. Following the AI-proposed design, electrodes were manufactured and developed into coin half-cells to test experimentally the predictive ability of the Alchemite. The target aims to produce electrodes with increased aerial capacities for high-energy-density applications. We used a data-driven Bayesian method of formulation optimization to take advantage of the machine-learning model's learned relationships between input and measured properties: traditional experimental design techniques, being purely focused on an exploration of the formulation space, are not able to leverage complex nonlinear relationships between variables. Alchemite, by contrast, prioritizes experimental effort based on probable performance and so is able to respond to existing experimental data to target only those formulations most likely to succeed against a project's goals. Again, a GPR was applied to all the data using an RBF kernel with length scale set to the standard deviation of the independent variable for each plot. [Figure 8A](#) shows that current cells with active mass greater than 20 mg are unable to achieve

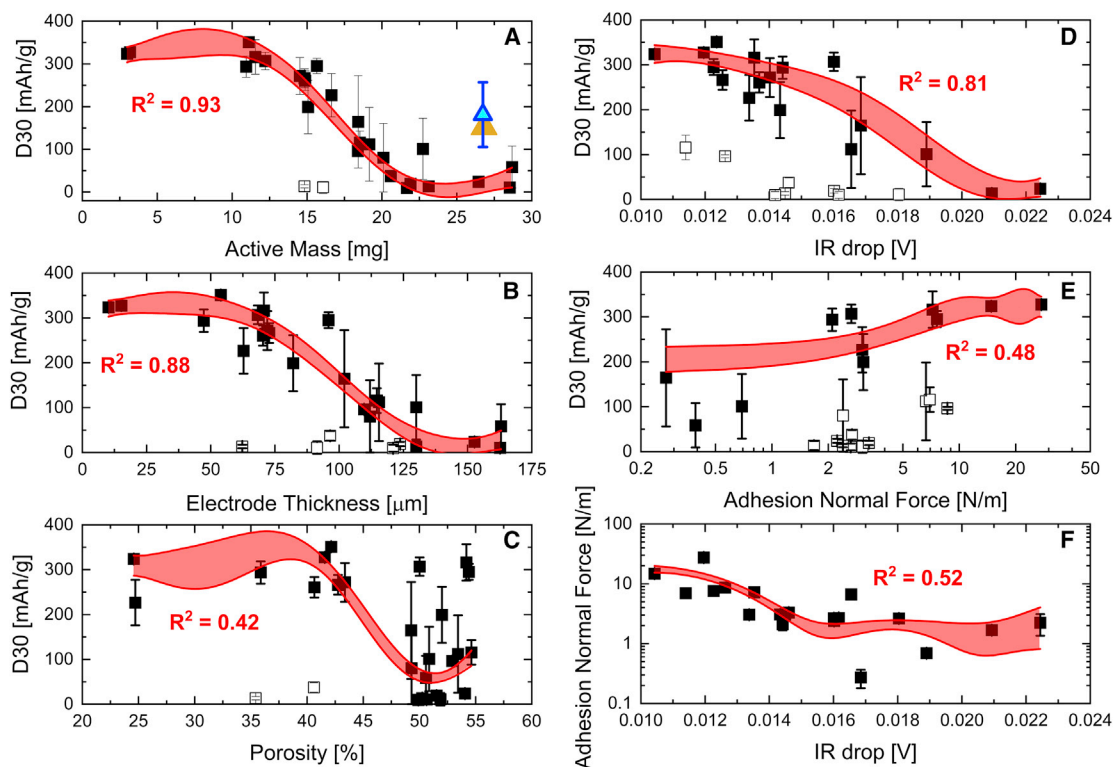


Figure 8. Physical properties and Alchemite predictive tools toward cycle life performance

(A–E) Discharge-specific capacity at the 30th cycle (D30) as a function of (A) active mass, (B) electrode thickness, (C) porosity, (D) IR drop (obtained from the first cycle after formation), and (E) adhesion normal force.

(F) The dependence of adhesion normal force from the IR drop. With black symbols are the experimental data (closed symbols correspond to data that were used for the GPR red area fittings and open symbols were considered outliers). The blue and orange symbols are the predicted data of the optimized cell computed by the Alchemite model and the experimentally manufactured cell based on the Alchemite design, respectively. The characteristics of the Alchemite-designed electrodes (both prediction and experimental) are given at Table S5. The R^2 values of the GPR fittings are included in each graph.

The error bars are calculated based on the standard deviation.

D30 of over 150 mA.h/g, and so a cell with these properties will be a valuable contribution to the state of the art. The model also generates predictions for the other physical properties of the designed cell beyond the D30, based on the proposed formulation and manufacturing processes. The key model predictions are shown by blue triangles in Figure 8, with error bars indicating the single standard deviation prediction intervals from the model. Based on the Alchemite design, electrodes were manufactured to verify the prediction experimentally. The prediction was design based on the cycle life performance, with slurry rheology information to be implemented in the Alchemite model in the future.

Figure 8 provides evidence between the associations of several parameters that govern the electrochemical performance of a Li-ion anode half-cell to obtain a better insight into the fabrication-performance relationship. The discharge-specific capacity (D30) is employed throughout Figure 8 because it “carries” information about both the cycle life and the initial capacity. The solid symbols are data that were taken into account for the GPR fittings, including errors (red areas), and the open symbols correspond to cells that exhibited very low D30 values and thus deviated significantly from the trends, so they were not part of the fittings.

In Figures 8A and 8B, D30 appears to have a sigmoidal relationship with the active mass and the electrode thickness, indicating that, for better-performing cells, low active mass and thickness are preferable, an effect that is attributed to faster lithiation and delithiation.²⁶ A different formulation and manufacturing protocol than the experimentally examined dataset, presented in Table S5, is expected to lead to a much-improved D30 performance at high active mass, as it is apparent from the data-driven cell (blue triangular symbol). At this active mass, it is observable that the experimentally produced dataset cells exhibit less than half D30 values. According to Table S5, considerably lower amount of C45 is required for the predicted cell, which also diminishes the necessity for higher binders' amount, an observation that is in agreement with the literature.⁵⁶ Thus, the graphite content is higher (in total increased by 3.5% w/w comparing to most cases), resulting in reduced electrical resistances, from which thicker electrodes usually suffer. Indeed, the IR drop values extracted from the cells based on the AI-designed electrodes were found to be 12.7 ± 2.6 mV, significantly less than other cells of similar active mass. The experimentally developed electrodes based on the AI-designed predictions (orange triangular symbol) yield cells with D30 values very close to the predictions and above 150 mA.h/g for over 25 mg, leading thus to a successful verification of the Alchemite predictions. In addition, the AI-designed cells exhibited at least 2.5 times higher D30 values than the other experimentally tested cells of similar active mass, as seen in Figure 8A. A comparison between the Alchemite prediction cell and the experimentally developed one based on the AI design is given in Table S6. Figure 8C shows the effect of porosity, which significantly deteriorates the performance after the critical point of 50%, due to the increase of resistance that comes with porosity.²⁸ Below 37% porosity, a slight decrease is also observable in the performance, indicating that the size of the pores is significant for lithiation and delithiation.

Figure 8D presents the dependence of D30 from the IR drop, as this is calculated from the first cycle after the formation step. A sigmoidal trend is also observed, showing that the lower the IR drop, the better the performance is (higher D30 values), as a result of the lower resistance of the coated electrode.⁵⁷ To designate the predictive part of the present work, a connection between electrochemical properties and adhesion tests (independent mechanical measurement) is drawn and presented in Figure 8E. The relationship between D30 and logF is close to linear and confirms that adhesion is an important property for the prediction of the electrochemical performance and that, with adhesion testing, the cell optimization can be done more efficiently without doing the time-consuming formation and cycling tests.³⁰ Finally, a relationship between the IR drop and adhesion normal force is also visible, indicating a strong dependence between adhesion properties and the internal resistance of the cell according to Figure 8F, with the data-driven predicted cell to also exhibit this dependence.

DISCUSSION

The aim of this work was to establish connections between the early physical properties observed during the manufacturing processes of thick graphite electrodes for Li-ion batteries and their corresponding cycle life performance. Knowledge of these connections will facilitate the optimization of the manufacturing process in electrode development in a time-efficient way and thus use them as predictive tools to avoid the time-consuming and costly electrochemical testing. To achieve this aim, 27 different formulation and manufacturing protocols designed for high-energy applications were prepared and tested, aiming to optimize their cycle life performance.

The examined cases included variations in the CMC:SBR ratio, different additives, changes in the coating and drying conditions (blade gap size, speed, and temperature), and the effect of calendaring. The cell information and testing performance were employed to train a data-driven model (Alchemite) that was later validated successfully against experimental data that were not part of the training dataset. The Alchemite model was then used to predict new formulation and manufacturing conditions to predict electrodes with better capacity retention at higher thicknesses than those experimentally developed. The electrode formulation calculated by the data-driven model was characterized by low binder and carbon black concentrations, resulting in higher graphite content that was found to be beneficial to cycle life performance.

The research presented here establishes that there are indeed connections between the electrode's physical properties and the electrochemical cycling response. In particular, the two parameters that were observed to affect the capacity retention the most were the adhesion normal force and the IR drop and were found to have an inverse correlation with each other, with high adhesion forces to yield low internal cell resistances and vice versa. Both properties can be measured at an early stage of cell development, after drying (or calendaring if applied) for the adhesion testing and after electrochemical formation for the IR drop calculation. Finally, the Alchemite-predicted electrode yielded an improved cycle life performance characterized by a formulation outside the experimental dataset used for training, indicating the predictive capabilities of data-driven models. We have shown that, with the data provided, the model provides robust agreement and can also predict results. However, with limited datasets, often not all the required input factors are included in the model, as they have limited effect upon the end result. For example, processability relies heavily upon rheological properties but may have little effect upon the final performance parameters. A DOE would provide more accurate data into the model. With new materials and chemistries, the parameter boundaries for processing are often not known. These boundaries can be very abrupt, with an instantaneous "fail" past certain limits; this is difficult to predict. Still, significant trial and error or empirical design is required to test these boundaries to obtain sensible process windows.

This work shows that small datasets can be used for optimization of manufacturing processes, although further work is required to expand the dataset further, particularly for different formulations, in order to achieve improved optimization of high-coat-weight graphite electrodes.

EXPERIMENTAL PROCEDURES

Resource availability

Lead contact

Further information and requests for resources and materials should be directed and will be fulfilled by the lead contact, Emma Kendrick (e.kendrick@bham.ac.uk).

Materials availability

This study did not generate new unique reagents.

Data and code availability

Raw data and the Alchemite configuration files are supplied and can be found at <https://doi.org/10.17632/4dh2h3tsf4.1> (<https://data.mendeley.com/datasets/4dh2h3tsf4/draft?a=301e2177-92bf-4929-899f-ef53d9ae956f>).

Artificial intelligence

The first step is for Alchemite to input the 31 formulation descriptors of each cell and any available experimental endpoints. The Alchemite machine-learning algorithm will exploit available endpoint values to predict other missing endpoints, so Alchemite requires estimates for any absent endpoints for the internal neural network. To accomplish this, the second step of the Alchemite algorithm is to impute estimates for those missing values, using the *a priori* simplest possible estimate: the average of all values in the training set for that endpoint.

The input data are now prepared, and so the third stage is to use these values as an input for a neural network. The parameters of the neural network are optimized as model hyperparameters. This neural network will identify the descriptor-endpoint as well as the endpoint-endpoint correlations to improve the quality of predictions, especially when extrapolating. The neural network makes predictions for all endpoints and is explicitly orthogonal to the identity so never uses a given endpoint to predict its own value. 200 neural networks are trained within a standard bootstrap phenomenology with different weights on each row of the training data.⁴⁸ Each neural network makes a separate prediction, and the average is used as the output value of the endpoint, with the standard deviation between them acting as an estimate of the uncertainty in the prediction of the endpoint.

The predictions from the neural network impute the gaps in the originally sparse endpoint data. These predictions replace the original mean value estimates for the missing endpoints. The cycle is repeated with the endpoint predictions at each pass softened by merging them with the previous estimate, $z^{n+1} = \gamma z^n + (1 - \gamma)y^{n+1}$, where z^n denotes the prediction from the n th iteration, y^{n+1} the prediction from the $(n + 1)$ th iteration, and the softening parameter γ is a hyperparameter. The iterative cycles are repeated until the predictions converge within an accuracy specified by a model hyperparameter. Uncertainty is propagated within the model so that the more confident model predictions are assigned more credence when using them as input in subsequent iterative cycles.

Alchemite handles functional relationships (for example, capacity as a function of cycle number) as a single entity by storing their entries as a vector. Alchemite stores the functional relationship across two columns in its database, corresponding to the abscissa and ordinate. Each entry in the database comprises a list of points, corresponding to all data for the functional relationship. Then, when making predictions for the functional relationship, Alchemite cycles through all abscissa values to make predictions for the ordinate endpoints individually.

Alchemite has several hyperparameters that can be set when training the model that will affect its performance. The training hyperparameters were tuned automatically by a Bayesian Tree Parzen Estimator algorithm to optimize for the median coefficient of determination, computed using 5-fold cross-validation of the training dataset, across the cell target properties that the model will be asked to predict.⁵⁸ In cross-validation, the model achieved a median coefficient of determination of 0.81, with a range from 0.87 (for the “test: capacity (max)” property) through 0.83 (for the “test: capacity vs cycle (gravimetric)” property) to -0.03 (for the “test: efficiency vs cycle” property). This approach tests the real-world prospective application of the model to predicting the performance of potential future cells based on past cell data. For testing, the model was asked to predict the target properties for each cell in the hold-out dataset given only the descriptor properties (input only properties and process parameters, such as active mass, anode and cathode

thickness, gap size, coating temperature, additives, binders, solvents, etc.). Then, the coefficient of determination for each target property was calculated by comparing the predicted values with the given ones.

The optimized cell shown in [Figure 8](#) was determined by searching over the space of possible design parameters using a Bayesian Tree Parzen Estimator algorithm.⁵⁸ At each iteration of the search, Alchemite predicts the target properties for the given set of proposed design parameters and then, taking into account the uncertainty of the prediction, computes the probability that the proposed cell will meet the required targets. It is this probability that the cell is optimized for.

The formulation and processing parameter space that Alchemite explores is constrained to ensure that the resulting cells are manufacturable and realistic. The independent variables of the design space (a subset is listed in [Table S5](#)) were constrained to lie within the range of values seen in the training data, and the dependent variables were either calculated analytically on the fly (where an analytical relationship is known—e.g., the anode density as a ratio of its mass and volume) or predicted using the multi-output machine-learning model. The active mass of the cell was additionally constrained to be above 25 mg, which, as shown in [Figure 8A](#), is higher than used in typical high-capacity cells of this type, providing a challenging constraint for the machine learning but a valuable direction for future cell development.

SUPPLEMENTAL INFORMATION

Supplemental information can be found online at <https://doi.org/10.1016/j.xcrp.2021.100683>.

ACKNOWLEDGMENTS

All the authors would like to acknowledge the Innovate UK Faraday Challenge Competition for funding under project no. 133855. C.D.R. and E.K. acknowledge financial support from The Faraday Institution, NEXTRODE project (<https://faraday.ac.uk>; EP/S003053/1), grant number FIRG015. K.B.O. and E.K. acknowledge financial support from The Faraday Institution, MSM project (<https://faraday.ac.uk>; EP/S003053/1), grant numbers FITG011 and FIRG003. G.J.C. acknowledges financial support from the Royal Society.

AUTHOR CONTRIBUTIONS

Conceptualization, E.K.; data curation, P.M., R.C.P., G.W., T.M.W., G.J.C., and A.C.; formal analysis, S.X.D., A.G.-S., P.M., R.C.P., K.B.O., G.W., T.M.W., G.J.C., and A.C.; funding acquisition, E.K. and A.C.; investigation, S.X.D., A.G.-S., C.D.R., D.L.B., and B.P.; methodology, S.X.D., A.G.-S., P.D., R.C.P., and E.K.; project administration, A.C. and E.K.; resources, R.C.P., A.C., and E.K.; software, P.M., R.C.P., G.W., T.M.W., G.J.C., and A.C.; supervision, E.K.; validation, S.X.D., A.G.-S., R.C.P., C.D.R., T.M.W., and G.J.C.; visualization, S.X.D. and E.K.; writing – original draft, S.X.D. and E.K.; writing – review & editing, S.X.D., R.C.P., C.D.R., D.L.B., K.B.O., T.M.W., G.J.C., and E.K.

DECLARATION OF INTERESTS

R.C.P., T.M.W., and G.J.C. are employees of Intellegens, which develops the Alchemite machine learning software. P.M., G.W., and A.C. are employees of Ansys

UK, which develops the Ansys Granta MI software, used to develop the centralized cells information database.

Received: July 1, 2021

Revised: October 19, 2021

Accepted: November 17, 2021

Published: December 7, 2021

REFERENCES

- Goodenough, J.B., and Park, K.-S. (2013). The Li-ion rechargeable battery: a perspective. *J. Am. Chem. Soc.* *135*, 1167–1176.
- Yoshino, A. (2012). The birth of the lithium-ion battery. *Angew. Chem. Int. Ed. Engl.* *51*, 5798–5800.
- Rubio Lopez, I., Lain, M.J., and Kendrick, E. (2020). Optimisation of formation and conditioning protocols for lithium-ion electric vehicle batteries. *Batter. Supercaps* *3*, 900–909.
- Lyu, Y., Liu, Y., Cheng, T., and Guo, B. (2017). High-throughput characterization methods for lithium batteries. *J. Mater.* *3*, 221–229.
- He, J., Bahr, J., Chisholm, B.J., Li, J., Chen, Z., Balbyshev, S.N., Bonitz, V., and Bierwagen, G.P. (2008). Combinatorial materials research applied to the development of new surface coatings X: a high-throughput electrochemical impedance spectroscopy method for screening organic coatings for corrosion inhibition. *J. Comb. Chem.* *10*, 704–713.
- Liu, P., Guo, B., An, T., Fang, H., Zhu, G., Jiang, C., and Jiang, X. (2017). High throughput materials research and development for lithium ion batteries. *J. Mater.* *3*, 202–208.
- Xiang, X.D., Sun, X., Briceño, G., Lou, Y., Wang, K.A., Chang, H., Wallace-Freedman, W.G., Chen, S.W., and Schultz, P.G. (1995). A combinatorial approach to materials discovery. *Science* *268*, 1738–1740.
- Kendrick, E. (2019). CHAPTER 11. Advancements in manufacturing. In *Future Lithium-Ion Batteries*, A. Eftekhari, ed. (Royal Society of Chemistry), pp. 262–289.
- de las Casas, C., and Li, W. (2012). A review of application of carbon nanotubes for lithium ion battery anode material. *J. Power Sources* *208*, 74–85.
- Wang, C.-W., Yi, Y.-B., Sastry, A.M., Shim, J., and Striebel, K.A. (2004). Particle compression and conductivity in Li-ion anodes with graphite additives. *J. Electrochem. Soc.* *151*, A1489.
- Li, N., Chen, Z., Ren, W., Li, F., and Cheng, H.-M. (2012). Flexible graphene-based lithium ion batteries with ultrafast charge and discharge rates. *Proc. Natl. Acad. Sci. USA* *109*, 17360–17365.
- Chung, S.-Y., Bloking, J.T., and Chiang, Y.-M. (2002). Electronically conductive phosphoolivines as lithium storage electrodes. *Nat. Mater.* *1*, 123–128.
- Flandrois, S., and Simon, B. (1999). Carbon materials for lithium-ion rechargeable batteries. *Carbon* *37*, 165–180.
- Rezqita, A., Hamid, R., Schwarz, S., Kronberger, H., and Trifonova, A. (2015). Conductive additive for Si/mesoporous carbon anode for Li-ion batteries: commercial graphite vs carbon black C65. *ECS Trans.* *66*, 17–27.
- Dresselhaus, M.S., Dresselhaus, G., and Saito, R. (1995). Physics of carbon nanotubes. *Carbon* *33*, 883–891.
- Zhang, Y., Zhang, X.G., Zhang, H.L., Zhao, Z.G., Li, F., Liu, C., and Cheng, H.M. (2006). Composite anode material of silicon/graphite/carbon nanotubes for Li-ion batteries. *Electrochim. Acta* *51*, 4994–5000.
- Endo, M., Kim, Y.A., Hayashi, T., Nishimura, K., Matusita, T., Miyashita, K., and Dresselhaus, M.S. (2001). Vapor-grown carbon fibers (VGCFs): basic properties and their battery applications. *Carbon* *39*, 1287–1297.
- Bai, L.-Z., Zhao, D.-L., Zhang, T.-M., Xie, W.-G., Zhang, J.-M., and Shen, Z.-M. (2013). A comparative study of electrochemical performance of graphene sheets, expanded graphite and natural graphite as anode materials for lithium-ion batteries. *Electrochim. Acta* *107*, 555–561.
- Rynne, O., Dubarry, M., Molson, C., Nicolas, E., Lepage, D., Prébé, A., Aymé-Perrot, D., Rochefort, D., and Dollé, M. (2020). Exploiting materials to their full potential, a Li-ion battery electrode formulation optimization study. *ACS Appl. Energy Mater.* *3*, 2935–2948.
- Moretti, A., Kim, G.-T., Bresser, D., Renger, K., Paillard, E., Marassi, R., Winter, M., and Passerini, S. (2013). Investigation of different binding agents for nanocrystalline anatase TiO₂ anodes and its application in a novel, green lithium-ion battery. *J. Power Sources* *221*, 419–426.
- Nirmale, T.C., Kale, B.B., and Varma, A.J. (2017). A review on cellulose and lignin based binders and electrodes: Small steps towards a sustainable lithium ion battery. *Int. J. Biol. Macromol.* *103*, 1032–1043.
- Harper, G., Sommerville, R., Kendrick, E., Driscoll, L., Slater, P., Stolkin, R., Walton, A., Christensen, P., Heidrich, O., Lambert, S., et al. (2019). Recycling lithium-ion batteries from electric vehicles. *Nature* *575*, 75–86.
- Zhang, R., Yang, X., Zhang, D., Qiu, H., Fu, Q., Na, H., Guo, Z., Du, F., Chen, G., and Wei, Y. (2015). Water soluble styrene butadiene rubber and sodium carboxyl methyl cellulose binder for ZnFe₂O₄ anode electrodes in lithium ion batteries. *J. Power Sources* *285*, 227–234.
- Liu, G., Zheng, H., Song, X., and Battaglia, V.S. (2012). Particles and polymer binder interaction: a controlling factor in lithium-ion electrode performance. *J. Electrochem. Soc.* *159*, A214–A221.
- Kraytsberg, A., and Ein-Eli, Y. (2016). Conveying advanced Li-ion battery materials into practice: the impact of electrode slurry preparation skills. *Adv. Energy Mater.* *6*, 1600655.
- Zhao, R., Liu, J., and Gu, J. (2015). The effects of electrode thickness on the electrochemical and thermal characteristics of lithium ion battery. *Appl. Energy* *139*, 220–229.
- Laue, V., Röder, F., and Krewer, U. (2019). Joint structural and electrochemical modeling: Impact of porosity on lithium-ion battery performance. *Electrochim. Acta* *314*, 20–31.
- Shim, J., and Striebel, K.A. (2003). Effect of electrode density on cycle performance and irreversible capacity loss for natural graphite anode in lithium-ion batteries. *J. Power Sources* *119–121*, 934–937.
- Sheng, Y., Fell, C.R., Son, Y.K., Metz, B.M., Jiang, J., and Church, B.C. (2014). Effect of calendaring on electrode wettability in lithium-ion batteries. *Front. Energy Res.* *2*, 56.
- Baunach, M., Jaiser, S., Schmelzle, S., Nirschl, H., Scharfer, P., and Schabel, W. (2016). Delamination behavior of lithium-ion battery anodes: Influence of drying temperature during electrode processing. *Dry. Technol.* *34*, 462–473.
- Habedank, J.B., Günter, F.J., Billot, N., Gilles, R., Neuwirth, T., Reinhart, G., and Zaeh, M.F. (2019). Rapid electrolyte wetting of lithium-ion batteries containing laser structured electrodes: in situ visualization by neutron radiography. *Int. J. Adv. Manuf. Technol.* *102*, 2769–2778.
- Westphal, B., Bockholt, H., Günther, T., Haselrieder, W., and Kwade, A. (2015). Influence of convective drying parameters on electrode performance and physical electrode properties. *ECS Trans.* *64*, 57–68.
- Meyer, C., Bockholt, H., Haselrieder, W., and Kwade, A. (2017). Characterization of the calendaring process for compaction of electrodes for lithium-ion batteries. *J. Mater. Process. Technol.* *249*, 172–178.
- Mukerjee, R., and Jeff Wu, C.F. (2006). *A Modern Theory of Factorial Designs* (Springer).
- Duquesnoy, M., Lombardo, T., Chouchane, M., Primo, E.N., and Franco, A.A. (2020). Data-driven assessment of electrode calendaring process by combining experimental results, *in silico* mesostructures

- generation and machine learning. *J. Power Sources* 480, 229103.
36. Aykol, M., Herring, P., and Anapolosky, A. (2020). Machine learning for continuous innovation in battery technologies. *Nat. Rev. Mater.* 5, 725–727.
 37. Pan, H., Lü, Z., Wang, H., Wei, H., and Chen, L. (2018). Novel battery state-of-health online estimation method using multiple health indicators and an extreme learning machine. *Energy* 160, 466–477.
 38. Bhowmik, A., and Vegge, T. (2020). AI fast track to battery fast charge. *Joule* 4, 717–719.
 39. Turetskyy, A., Thiede, S., Thomitzek, M., von Drachenfels, N., Pape, T., and Herrmann, C. (2020). Toward data-driven applications in lithium-ion battery cell manufacturing. *Energy Technol.* 8, 1900136.
 40. Liu, Y., Zhang, R., Wang, J., and Wang, Y. (2021). Current and future lithium-ion battery manufacturing. *iScience* 24, 102332.
 41. Cunha, R.P., Lombardo, T., Primo, E.N., and Franco, A.A. (2020). Artificial intelligence investigation of NMC cathode manufacturing parameters interdependencies. *Batter. Supercaps* 3, 60–67.
 42. Wu, B., Widanage, W.D., Yang, S., and Liu, X. (2020). Battery digital twins: perspectives on the fusion of models, data and artificial intelligence for smart battery management systems. *Energy AI* 1, 100016.
 43. Jia, Y., Li, J., Yuan, C., Gao, X., Yao, W., Lee, M., and Xu, J. (2021). Data-driven safety risk prediction of lithium-ion battery. *Adv. Energy Mater.* 11, 2003868.
 44. Ng, M.-F., Zhao, J., Yan, Q., Conduit, G.J., and Seh, Z.W. (2020). Predicting the state of charge and health of batteries using data-driven machine learning. *Nat. Mach. Intell.* 2, 161–170.
 45. Conduit, B.D., Jones, N.G., Stone, H.J., and Conduit, G.J. (2017). Design of a nickel-base superalloy using a neural network. *Mater. Des.* 131, 358–365.
 46. Whitehead, T.M., Irwin, B.W.J., Hunt, P., Segall, M.D., and Conduit, G.J. (2019). Imputation of assay bioactivity data using deep learning. *J. Chem. Inf. Model.* 59, 1197–1204.
 47. Verpoort, P.C., MacDonald, P., and Conduit, G.J. (2018). Materials data validation and imputation with an artificial neural network. *Comput. Mater. Sci.* 147, 176–185.
 48. Efron, B. (1979). Bootstrap methods: another look at the jackknife. *Ann. Stat.* 7, 1–26.
 49. Gorman, S.F., Pathan, T.S., and Kendrick, E. (2019). The “use-by date” for lithium-ion battery components. *Philos. Trans. R. Soc. A Math. Phys. Eng. Sci.* 377, 20180299.
 50. Buqa, H., Holzapfel, M., Krumeich, F., Veit, C., and Novák, P. (2006). Study of styrene butadiene rubber and sodium methyl cellulose as binder for negative electrodes in lithium-ion batteries. *J. Power Sources* 161, 617–622.
 51. Guy, D., Lestriez, B., Bouchet, R., Gaudefroy, V., and Guyomard, D. (2005). Tailoring the binder of composite electrode for battery performance optimization. *Electrochem. Solid-State Lett.* 8, A17.
 52. Drogenik, J., Gaberscek, M., Dominko, R., Poulsen, F.W., Mogensen, M., Pejovnik, S., and Jamnik, J. (2003). Cellulose as a binding material in graphitic anodes for Li ion batteries: a performance and degradation study. *Electrochim. Acta* 48, 883–889.
 53. Sehwat, P., Julien, C., and Islam, S.S. (2016). Carbon nanotubes in Li-ion batteries: a review. *Mater. Sci. Eng. B* 213, 12–40.
 54. Doyle, M., Newman, J., Gozdz, A.S., Schmutz, C.N., and Tarascon, J.-M. (1996). Comparison of modeling predictions with experimental data from plastic lithium ion cells. *J. Electrochem. Soc.* 143, 1890.
 55. Buqa, H., Goers, D., Holzapfel, M., Spahr, M.E., and Novák, P. (2005). High rate capability of graphite negative electrodes for lithium-ion batteries. *J. Electrochem. Soc.* 152, A474.
 56. Marks, T., Trussler, S., Smith, A.J., Xiong, D., and Dahn, J.R. (2011). A guide to Li-ion coin-cell electrode making for academic researchers. *J. Electrochem. Soc.* 158, A51.
 57. Abe, Y., Hori, N., and Kumagai, S. (2019). Electrochemical impedance spectroscopy on the performance degradation of LiFePO₄/graphite lithium-ion battery due to charge-discharge cycling under different C-rates. *Energies* 12, 4507.
 58. Bergstra, J., Bardenet, R., Bengio, Y., and Kégl, B. (2011). Algorithms for hyper-parameter optimization. In *Proceedings of the 24th International Conference on Neural Information Processing Systems* (Curran Associates), pp. 2546–2554.